Causal Model of an Industrial Platinum Flotation Circuit

Chris Steyn[a,*], Carl Sandrock[b]

[a]*Anglo American Platinum, 55 Marshall Street, Johannesburg, 2001, (email: chris.steyn@angloamerican.com)*
[b]*Department of Chemical Engineering, University of Pretoria, Pretoria, South Africa, (email: carl.sandrock@up.ac.za)*

Abstract

Models of flotation found in literature are generally complex and reliant on manual surveys and laboratory data. Furthermore, these models do not usually indicate the causal relationships from true process independent variables to process outputs such as individual cell recovery and metal grade. These models are often found to be suitable for design but less applicable to the simulation of an industrial plant to perform offline control and optimization studies. This study explains these relationships from the individual cell inputs, level and air valves, to cell hydrodynamics and ultimately mass produced, recovery and grade. A technique is proposed to derive individual cell froth recovery by adjusting one froth stability parameter across the entire bank. The model is trained on an industrial platinum concentrator using predominantly online plant data and the model predictions are compared to real plant data over a period of a month.

Keywords: Flotation Modelling, Flotation Causality, Froth Recovery

1. Introduction

The capital required to improve profit and drive large scale improvements is often lacking in a cyclical business like mining. One mechanism to continuously propel profit without such expense is to improve efficiency of the existing equipment. Mogalakwena North Concentrator (MNC) is the largest single stream Platinum Group Metals (PGM) Concentrator in the world. At such a scale, any efficiency improvements can therefore easily translate into large financial gain.

R.P. King [19] explains the benefits of a flotation process model when used to optimise performance. Several other researchers have confirmed such improvements through flotation optimisation and control studies using various derived models [1], [5], [22]. These models require extensive plant sampling and laboratory derived information which are not suitable for continuous online industrial scale optimization. Furthermore, many of these models require knowledge of the established process and does not explain the causal flow of information. The objective of this research project is to construct a model of the MNC primary flotation circuit to use in an offline simulation to perform circuit-wide control design and optimization. It was therefore necessary to correctly interpret the causal flow of information in the flotation model [1] from the true independent inputs of the circuit to the individual cell recovery and grade. To enable the use of the model in real time, the aim was to derive the model with minimal use of manual sampling and laboratory data. To test robustness, the model is trained and validated against real industrial data.

Froth recovery is required by the flotation model (6) and the subject of several studies cited in this literature review. Froth recovery is often characterized as complex, mostly due to the difficulty of measuring this parameter [30]. This study proposes a unique approach to train froth recovery, using the more elementary description by Dobby and Finch [9] and the dynamic froth stability defined by Bikerman [7]. The method requires the fitting of one parameter for the entire bank, the froth stability calibration parameter (c), that manipulates the grade profile down the bank according to measured froth stability characteristics.

*Corresponding author

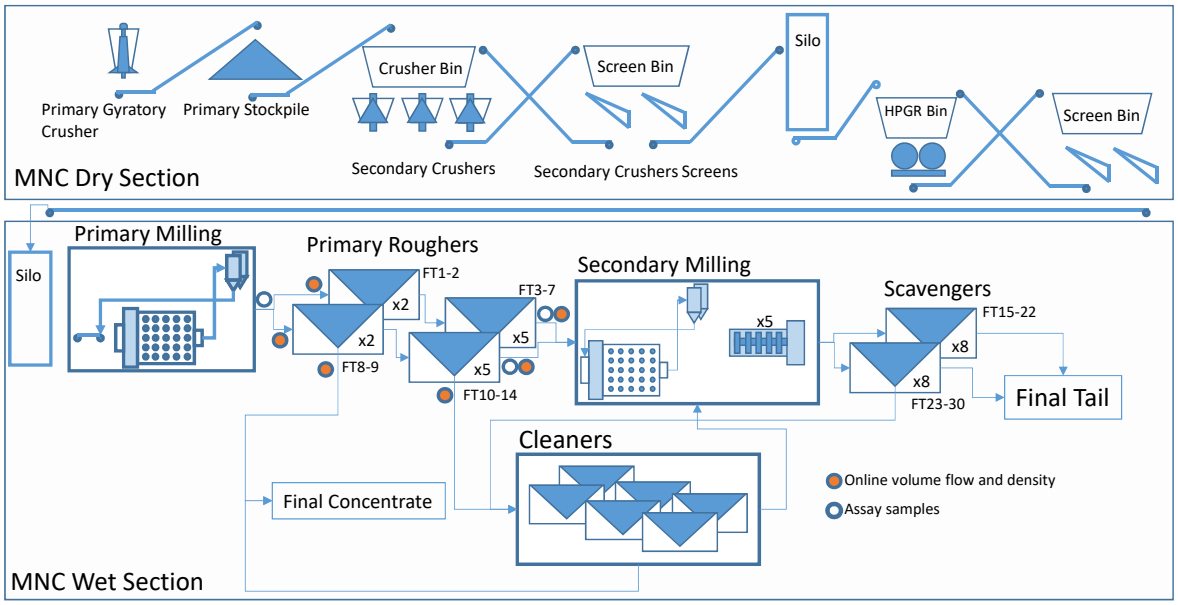

Figure 1: Simplified process flow diagram of the MNC wet circuit.

Section 2 provides a summary of the MNC circuit process flow. A literature survey into the kinetics of flotation and the flotation model, together with peripheral studies, is discussed in Section 3. An explanation of the flotation model's causal flow of data and the proposed training of froth recovery, follows in Section 4. The results of the model which is trained on real MNC data over a period of a month and tested over 7 days is shown and discussed in Section 5.

2. Process Description

MNC's primary mill is fed crushed ore at a top size of 8 mm from a dry crushing plant. The crushing circuit consists of a truck fed gyratory primary crusher, three 650 kW cone crushers and a single high pressure grinding rig (HPGR). MNC employs a typical mill-float-mill-float (MF2) configuration with two 26 ft ball mills, one for primary duty and the other, together with 5 IsaMills^{TM}, making up the secondary duty (Fig. 1). The primary comminution circuit feeds two parallel primary rougher flotation banks, each containing seven 100 m^3 tank cells. The cells on the first bank are named FT1 to FT07 while the cells on the second parallel bank are named FT08 to FT14. Cells FT01 and FT02 are forced air Dorr-Oliver cells with FT03 to FT07 being naturally aspirated Wemco Cells. Primary rougher cells FT08 to FT14 are all forced air Dorr-Oliver cells and the subject of the modelling discussed in this paper. The scavengers are also built in parallel banks of 2×8 cells with, FT15 to FT22 on the one side and FT23 to FT30 on the other. All the scavengers are forced Dorr-Oliver cells apart from FT17 to FT23, which are 5 naturally aspirated Wemco cells.

Modelling is focused on the second rougher bank that only contains forced air Dorr-Oliver cells (FT08 to FT14), illustrated by the dashed border in Fig. 2. The concentrate of the first two cells report to the final concentrate while the next 5 cells are sent to the cleaner sections. Volume flow rate, density and mass flow rate are measured on the feed $(q_F, \rho_F, \dot{m}_F)$ and tailings streams $(q_T, \rho_T, \dot{m}_T)$ of each bank. Volume flow rate, density and mass flow rate are also measured on the two product concentrate streams of each bank $(q_{Ck}, \rho_{Ck}, \dot{m}_{Ck}, k \in 1, 2)$. Composite samples over an 8 hour shift are taken at the combined feed to the banks and individual bank tail streams. These are analysed for particle size and various mineral concentrations. For the purpose of this study the platinum (Pt) and palladium (Pd) concentrations in the assay samples will be considered for the component balance ($g_{Pt,k}$ and $g_{Pd,k}$ where k denotes the particular

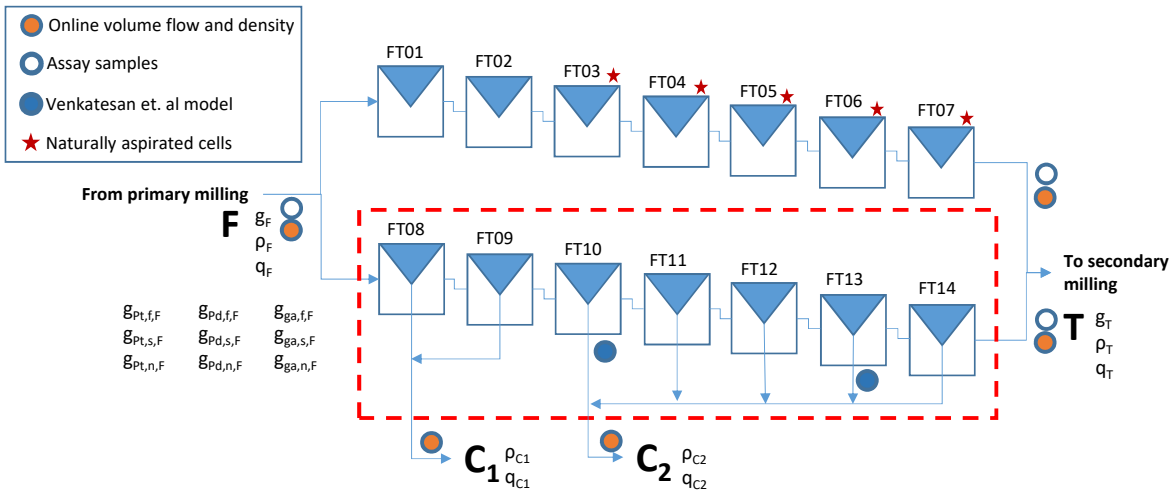

Figure 2: Mass balance boundary around the second primary rougher bank. Nine species are considered during the modelling, namely, platinum (Pt), palladium (Pd) and gangue (Ga), each divided into three floatable ranges: fast (f), slow (s) and non-floating (n).

stream). The rest of the mineral species in the pulp is considered gangue ($g_{ga,k}$). The air flow rate ($q_{air,n}$) and froth depth (h_n) on each cell are measured and controlled where n denotes the particular cell (Fig. 3). Various froth parameters are also measured by Stone Three Froth Cameras (S3FC) and the associated variables of importance for this study are the froth height above the free surface (Z_n) and the froth velocity at the free surface (u_n).

3. Literature Review

3.1. Flotation Kinetics

Arbiter and Harris [2] used a first order chemical reaction in a continuous stirred tank reactor (CSTR) where a change in concentration over time is used as a model for flotation. Recovery for the continuous flotation cell is given by,

$$R = \frac{k\tau}{1 + k\tau} \tag{1}$$

where residence time τ is given by,

$$\tau = \frac{V_p}{q_p} \tag{2}$$

The cell volume and flow rate entering the pulp zone are represented by V_p and q_p respectively.

For the continuous process, Dobby and Finch [9] established an overall recovery for the continuous column cell. Their approach divided the flotation process into two zones, 1) the collection or pulp zone and 2) the cleaning or froth zone (Fig. 4) with each zone yielding a recovery: the recovery of the pulp zone R_c and the froth zone R_f. The recovery in the collection zone can be modelled by a first order rate process with k_c as the rate constant,

$$R = \frac{k_c \tau_c R_f}{1 + k_c \tau_c R_f} \tag{3}$$

Gorain et al. [11] defined the overall rate constant in (1) as,

$$k = p S_b R_f \tag{4}$$

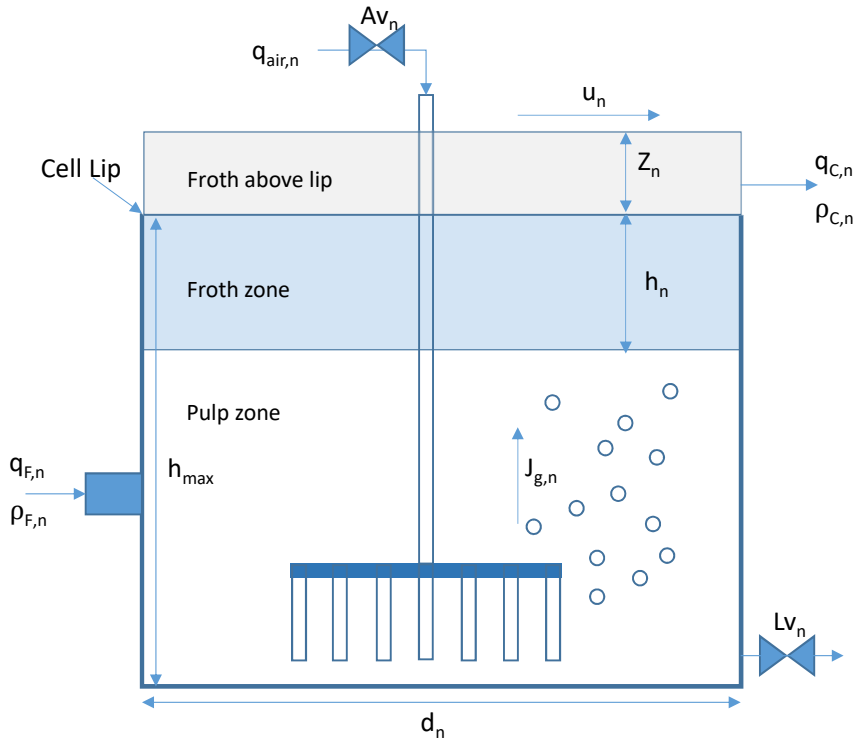

Figure 3: An illustration of a flotation cell indicating various parameters considered during the study.

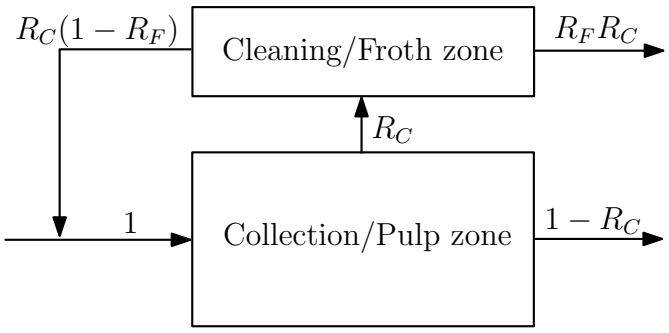

Figure 4: Interaction between the collection/pulp and cleaning/froth zones in a continuous flotation cell [9].

where p is the floatability of the ore and S_b the bubble surface area flux. The latter was defined by Gorain et al. [13] as,

$$S_b = \frac{6J_g}{d_{32}} \tag{5}$$

with J_g defined as the superficial gas velocity [12] and d_{32} the Sauter mean bubble size in the pulp phase [13]. Both of these parameters were measured with the University of Cape Town (UCT) bubble sizer. Substituting equation (4) into (1) produces the recovery for true flotation,

$$R = \frac{pS_bR_f\tau_c}{1 + pS_bR_f\tau_c} \tag{6}$$

R_f is defined as the ratio of particles reporting to the concentrate via true flotation to the particles at the pulp-froth interface. Finch and Dobby [9] defined froth recovery as the ratio,

$$R_f = \frac{k}{k_c} \tag{7}$$

Gorain et al. [14] studied the effect of froth residence time on flotation kinetics to improve the understanding of froth recovery. Froth residence time (FRT) as a function of froth volume (V_f), slurry flow rate in the froth (q_f) and the gas hold-up in the froth phase ϵ_f was defined as,

$$FRT = \frac{(1 - \epsilon_f)\, V_f}{q_f} \tag{8}$$

Mathe et al. [20] used (8) in a review of non-steady state froth phases and derived flotation rate k in terms of the froth residence time [20],

$$k = k_c e^{-\beta FRT} \tag{9}$$

Mathe et al. [20] showed that the exponential factor, β, is dependent on chemical and physical properties of the froth. Substituting (9) into (7) produced the following derivation of froth recovery,

$$R_f = e^{-\beta FRT} \tag{10}$$

In a summary review of the model Vera et al. [30] describes β as "related to the rate at which bubbles are coalescing and breaking-up", in other words a froth stability parameter. Several other researchers have proposed a derivation of froth recovery and its associated parameters [20], [21], [25], [29] - [33]. All of these, however, require either extensive laboratory work or are empirically derived. None provide a mechanistic model or rely on easily obtainable measurements in order to determine R_f. Alves et al. [1], found that (10) fit their overall recovery test work well.

3.2. Air Recovery

Ventura-Medina and Cilliers [28] defined the fraction of air recovered to concentrate (α) as,

$$\alpha = \frac{\epsilon_f u_f Z w}{q_p} \tag{11}$$

where u_f is the froth velocity at the free surface, Z the froth height above the cell lip and w the lip length. Barbain et al. [4] proposed a dynamic froth stability (Σ), originally defined by Bikerman [7], as a function of froth recovered to concentrate versus the air flowrate into the cell,

$$\Sigma = \frac{V_f}{q_p} = \frac{ZA}{q_p} \tag{12}$$

where A represents the cell area.

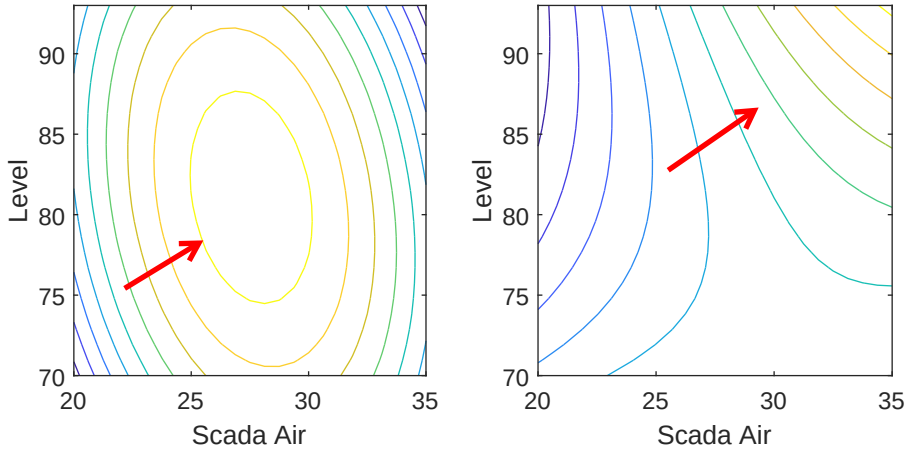

Figure 5: The response surface of a) 4-element(4E) PGM grade and b) mineral recovery to air addition (m/s) and cell level (%) on primary rougher cell FT10 (Venkatesan et al. [26]). The arrows indicate increasing grade and recovery, respectively.

Hadler and Cilliers [16] explored the significance of an inconsistency between the findings of Barbian et al. [3] and Ventura-Medina and Cilliers [28] on the effect of air recovery on flotation performance on four industrial flotation cells. Experiments confirmed an air recovery optimum to the amount of air induced into the cell, named, the Peak-Air-Recovery (PAR). However, not all the cells conformed to this observation, especially cells further down the bank. It was hypothesized that the stabilizing hydrophobic particles are mostly removed by the first three cells and so froth stability is reduced.

Hadler et al. [16] [17] expanded on the concept of PAR by also considering the flotation cell level or froth depth on an industrial scale. The results indicated a more complex three-dimensional relationship between air addition and froth depth to air recovery. This interactive relationship was further investigated by Venkatesan et al. [26] at MNC who were able to show the 3-dimensional mineral recovery and concentration planes of, amongst others, flotation cells FT10 and FT13 (Fig. 5).

3.3. Robust Statistics

It is commonly acknowledged that higher frequency on-line mineral processing data is contaminated with outliers due to the number of unmeasured parameters in the ore and measurement noise. The coefficient of determination (R^2) provides insight into the suitability of a particular model and can be misleading in the presence of outliers [24]. Robust regression is a set of techniques often utilized to provide more resilient results in the presence of outliers and does not make any assumption on the distribution of the prediction [8]. Robust statistics provide a goodness-of-fit measure upon the assumption that the model is merely an approximation of the process. The simplest approach is a method that only targets outliers in the y-direction or response direction (dependents). In its elementary form, samples where the predictions result in the highest residuals (r_i) are removed from the quality-of-fit calculation. Hydrodynamics results ($J_{g,n}$ and $d_{32,n}$) presented in this paper are low frequency experimentally sampled data and so the classic coefficient of determination can be used to determine model accuracy. Subsequent froth characteristic models, such as recovery and grade, rely on regression with on-line plant data ($\approx$1 /h) and therefore more resilient statistics to indicate model quality. The model statistics used in this paper are the more resilient statistics whereby 10 % of the samples with the highest residual values are removed and subsequently the relative root-mean-square-error (relative to the median of the parameter) and coefficient of correlation $RRMSE_{90}$ and R^2_{90} are

determined respectively. The $RRMSE_{90}$ for parameter P is given,

$$RRMSE_{90} = \frac{RMSE_{90,P}}{median(P)} \tag{13}$$

4. A Causal Model of Flotation

4.1. Causality

An outcome of this study is to use the model for predictive control and optimization. The causal flow of information within flotation literature, from the system independents, some of which can be utilized in control, to product recovery and grade had to be determined. Galles and Pearl [10] defines causal models used in engineering as, "a mathematical object that provides an interpretation of every causal query about the domain", with,

$$M = \langle U, V, F \rangle \tag{14}$$

where $V = \{V_1, ..., V_m\}$ are endogenous variables determined by the system (dependents), $U = \{U_1, ..., U_m\}$ are exogenous variables and F non-trivial functions $\{f_1 ..., f_n\}$. Yang et al. [32] differentiate between causality and connectivity in the context of process topology where the latter "relates to material and information flow connections between or within process units or sensors or actuators or controllers". The importance of process topology is emphasized as it determines the natural structure of distributed plant-wide control. Pearl [23] suggests that the investigator creates a causal diagram of the process topology to improve the understanding of the causal influences among variables. Fig. 6 illustrates such a causal flow for the flotation kinetic model reviewed in the literature study and discussed in subsequent sections. A nomenclature table with all the variables shown in Fig. 6 is provided in the Appendix. Note that the entire causal model of the one rougher flotation bank was built in Matlab® Simulink. All empirical parameters are derived iteratively using a minimization function (*fmincon*).

4.2. Exogenous Variables

The exogenous variables classified as disturbances in the system are primarily ore properties which include, but are not limited to, the mineral grades ($g_{i,F}$) and floatability of the mineral species (p_i) used in (6), particle size or grind, ore hardness as well as several others. The asterisk in the chart indicates that these ore properties affect most of the endogenous variables, the effect of which is not always known. Ore properties can to an extent be manipulated upstream in the milling circuit (grind and hence floatability) and mining operations (grade and mineralogy). For this study however, these variables remain disturbances. Reagent addition is also considered a disturbance exogenous variable which impacts most of the variables in the model. This study does however, not consider the effect of reagents changes.

Exogenous variables directly manipulated in the system are the individual flotation cell level and air valves (Lv_n, Av_n) as well as the solids feed and water flow rates ($\dot{m}_{s,F}$, $q_{w,n}$). The former are controlled by Proportional Integral Derivative (PID) controllers,

$$L_n = f_{PID,L}(Lv_n), \quad q_{air,n} = f_{PID,qair}(Av_n) \tag{15}$$

Note that the dynamic response time between the air and level valves and their respective measurements are between 30 sec and 2 min. Such a frequency is insignificant relative to the hourly execution rate of the model and are therefore not considered. The assumption is made that sufficient pseudo-steady-state periods exists within the process to characterize a steady-state model for higher level optimization. The model can therefore not be used for lower level control design. The solids and water feed flow rates condition the total volumetric flow (q_F) and density (ρ_F) to the flotation section. Total flow rate to the flotation section is then given by,

$$q_F = \frac{\dot{m}_{s,F}}{\rho_{s,F}} + q_{w,F} \tag{16}$$

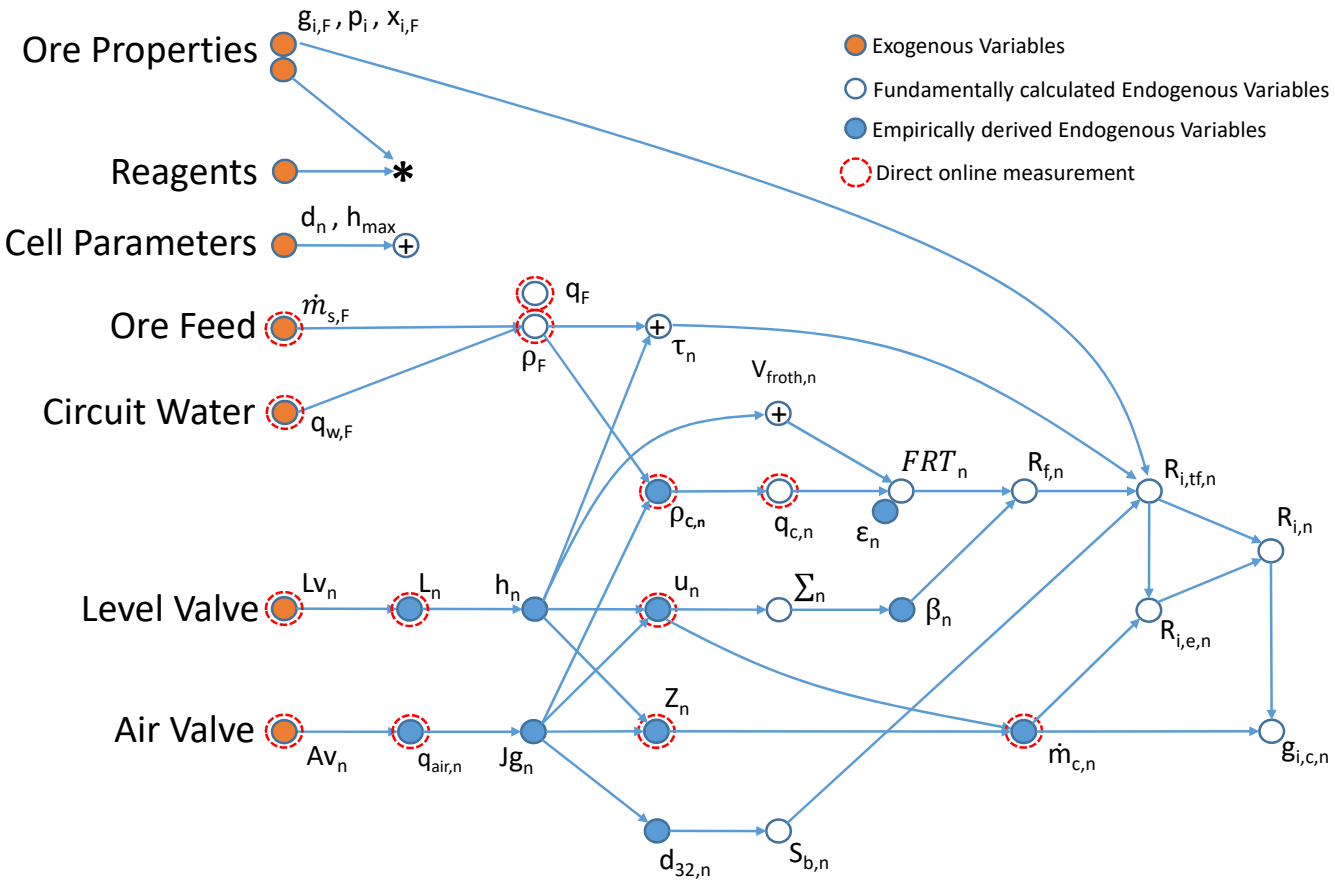

Figure 6: The causal diagram of the flotation model.

The bulk density, $\rho_{s,F}$ of the MNC ore is given as $3.2\,\mathrm{t/m^3}$ and the total feed density given by,

$$\rho_F = \frac{\dot{m}_F}{q_F} \tag{17}$$

and $\dot{m}_F = \dot{m}_{s,F} + q_{w,F}$.

4.3. Cell Hydrodynamics and Froth Characteristics

4.3.1. Froth Depth

The froth level to froth depth relationship (h_n) is found to be linear according to a calibration performed by site. This is given, relative to the level sensor reading, as $0\,\% = 600\,\mathrm{mm}$, $100\,\% = 0\,\mathrm{mm}$.

4.3.2. Pulp Residence Time (τ_n)

The residence time in the collection zone, as defined in (2), is calculated using the pulp volume and the volumetric flow through the cell. Note that the internal design factors of the flotation cell, for example, the shape of the cell, froth crowders, impeller volume etc., were considered during the construction of the causal model. However, to simplify the explanation, a cylindrical cell is used in (2),

$$\tau_n = \frac{V_{p,n}}{q_{F,n}} = \frac{\frac{\pi}{4} d_n^2 (h_{max} - h_n)}{q_{F,n}} \tag{18}$$

with d_n the internal cell diameter and h_{max} the total height of the cell.

4.3.3. Superficial Gas Velocity ($J_{g,n}$), Bubble Size ($d_{32,n}$) and Surface Flux ($S_{b,n}$)

The Anglo Platinum Bubble Sizer (APBS), was used to determine the relationship between the individual cell hydrodynamics ($J_{g,n}, d_{32,n}, S_{b,n}$) and the respective cell air on the seven cells in question, namely, FT08 to FT14. Venkatesan et al. [26], established linear models for $J_{g,n}$ and $d_{32,n}$ to air flow rate at MNC. Since cells FT08 and FT09 were sampled at more than one operating point during the time permitted, it was possible to determine more accurate models than those of FT10 to FT14, which were only sampled once. Fig. 7a shows the linear relationship of $J_{g,FT08}$ and $J_{g,FT09}$ to air flow, with R^2 values at 0.96 and 0.81 respectively, for sampling conducted during June 2019. Cells FT10 to FT14 were assumed to pass through point (0,0) in order to derive a linear model. Therefore,

$$J_{g,n} = m_{Jg,n} q_{air,n} + c_{Jg,n} \tag{19}$$

with $m_{Jg,n}$ the J_g slope parameter and $c_{Jg,n}$ the intercept of the J_g model. $c_{Jg,n} = 0$ for n = FT10 to FT14.

Bubble size in the pulp zone was also measured by the APBS and presented as the Sauter mean bubble size diameter. Regression with y-intercept at zero and only air produced acceptable models for d_{32} with $R^2 = 0.85$ for both FT08 and FT09. The $d_{32,n}$ models for cells FT10 to FT14 were also assumed to pass through the point (0,0),

$$d_{32,n} = m_{d32,n} q_{air,n} \tag{20}$$

for cells FT08 to FT14 with $m_{d32,n}$ the d_{32} slope parameter . The parameters $m_{Jg,n}$, $c_{Jg,n}$ and $m_{d32,n}$ for cells FT08 to FT14 are given in Table 1.

Table 1: Model parameters $m_{Jg,n}$ for $J_{g,n} = m_{Jg,n} q_{air,n}$ and $m_{d32,n}$ for $d_{32,n} = m_{d32,n} q_{air,n}$.

(1×10^{-3})		**FT08**	**FT09**	**FT10**	**FT11**	**FT12**	**FT13**	**FT14**
J_g	$m_{Jg,n}$	1.10	0.51	0.40	0.13	0.36	0.14	0.56
	$c_{d32,n}$	-0.018	0.004	0.00	0.00	0.00	0.00	0.00
d_{32}	$m_{d32,n}$	0.98	1.20	0.86	1.81	1.20	1.43	0.78

Bubble surface area flux ($S_{b,n}$) is calculated using (5) and the derived $J_{g,n}$ and $d_{32,n}$.

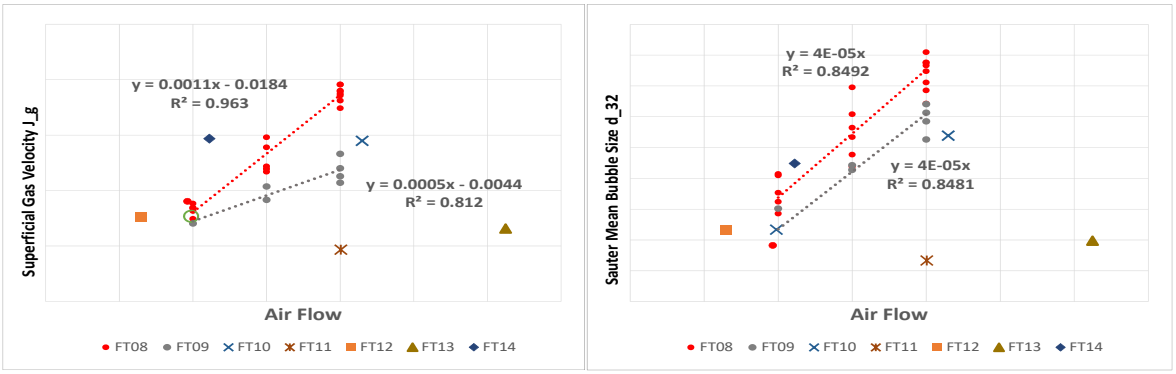

Figure 7: Exponential and linear model of air flow to a) J_g and b) d_{32}, respectively.

4.3.4. Froth Height (Z_n) and Froth Velocity (u_n)

MNC employs Stone Three Froth Cameras on all the mainstream flotation cells. The cameras are positioned close to the lip of each cell and provide a single point view of the froth velocity (u_n) and the height above the free surface (Z_n). Establishing predictions for these parameters using a mechanistic model was found to be complex and requires laboratory data not appropriate for the purpose of establishing a simplistic online model. Consequently, both the height above the lip, Z_n and the froth velocity at the free surface, u_n are measured and modelled by a base polynomial of the form,

$$Response = c_0 + c_1 P_1 + c_2 P_2 + c_3 P_1^2 + c_4 P_2^2 + c_5 P_1 P_2 \tag{21}$$

with parameters $P_1 \rightarrow J_g$ and $P_2 \rightarrow h$. However, to avoid a purely data-driven arbitrary model the forms of the froth characteristic models $u_n = f_{1,n}(J_{g_n}, h_n)$ and $Z_n = f_{2,n}(J_{g,n}, h_n)$ were constrained as follows — note that the frequency of data sampling is 1/h, which is significantly more than the process dynamics, which is therefore not considered,

1. **Top of Froth Velocity.** Movement of froth will come to a complete standstill when air to the cell is stopped. Froth velocity therefore tends towards zero as J_g tends towards zero, at any $h > 0$. The model therefore passes through the zero point $f_{1,n}(0, 0) = 0$. Also, as u remains zero $\forall h$ with no air present, any linear relationship of h to u will also be nullified. Since u is affected by the froth depth, an interaction term with J_g is expected. Froth velocity, or froth mobility, increases as J_g increases [16], $\frac{\partial u}{\partial J_g} > 0 \quad \forall \quad 0 \leq J_g \leq \infty$. It is expected that this relationship cannot remain linear and should eventually flatten and possibly reduce at higher air addition. Consequently, linear and second-order terms for J_g are expected in the model,

$$\hat{u}_n = a_{1,n} J_{g,n} + a_{3,n} J_{g,n}^2 + a_{5,n} J_{g,n} h_n \tag{22}$$

with $a_{2,n} < 0$ as the parabola opens downward and $a_{1,n} > 0$ to ensure that the vertex is positive. u_n decreases as froth depth increases, $\frac{\partial \hat{u}}{\partial h} < 0 \quad \forall \quad 0 \leq h \leq \infty$. $a_{5,n}$ is therefore expected to be negative as $\frac{\partial \hat{u}}{\partial h} = a_{5,n} J_{g,n} < 0$. An illustration of the model form is shown in Fig. 8. $\hat{u}$ is trained by minimizing an objective function (J_u) through iteratively changing coefficients a_n,

$$J_u = \sum (u_n - \hat{u}_n)^2 \tag{23}$$

2. **Height above the lip.** The deduction of the $\hat{Z}$ model form follows a similar argument as that of the PAR formulation [16]. As with $\hat{u}$ the formation of froth will stop completely if air flow is stopped. The height of the froth above the lip in the absence of air is therefore zero regardless of froth depth (other h terms cannot be reduced to zero as a higher order model is expected). Froth will start forming and

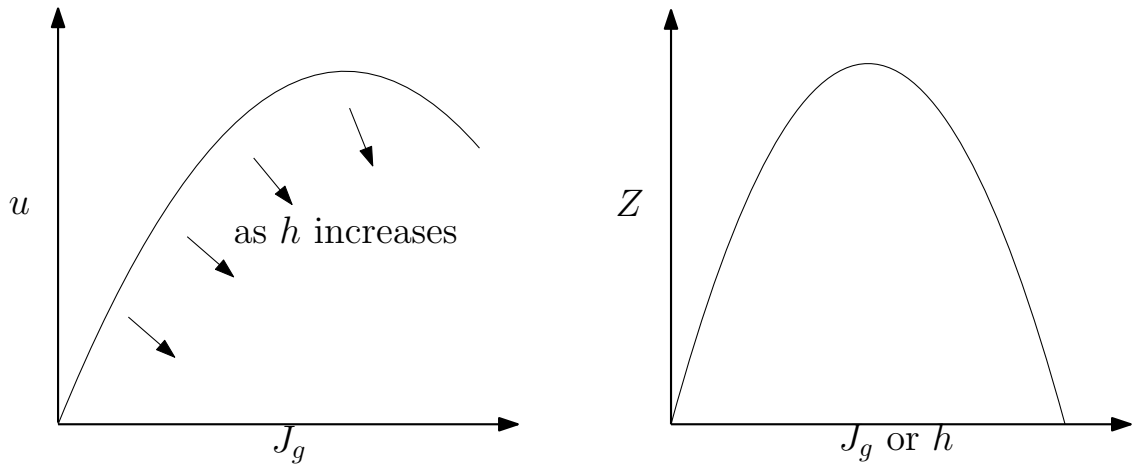

Figure 8: Simplified illustration of the model forms for u and Z.

continue to rise above the lip as air is introduced to the cell. Hadler and Cilliers [16] explains that S_b increases to promote froth formation but that the stability of the froth will ultimately deteriorate to a point where Z is again zero at higher air flow. A parabola-like shape was again observed by Hadler et al. [17] with regards to the effect of froth depth on air recovery. As air recovery is dependent on the froth height it is postulated that the effect of froth depth on Z will also be parabolic. Therefore, like the PAR, the height above the lip forms a parabola with a positive intercept (both J_g and h), opening downward. An interaction term is also expected,

$$\hat{Z}_n = b_{1,n}h_n + b_{2,n}J_{g,n} + b_{3,n}h_n^2 + b_{4,n}J_{g,n}^2 + b_{5,n}J_{g,n}h_n \tag{24}$$

with, $b_{3,n} < 0$, $b_{4,n} < 0$, $b_{1,n} > 0$ and $b_{2,n} > 0$. $\hat{Z}$ is trained by minimizing the objective function (J_Z) by iteratively changing the b_n coefficients,

$$J_Z = \sum (Z_n - \hat{Z}_n)^2 \tag{25}$$

4.4. Concentrate Mass Flow ($\dot{m}_n$)

The amount of froth mass flow generated by a flotation cell n is given as,

$$\dot{m}_{C,n} = \rho_{f,n}\left(1 - \epsilon_{f,n}\right) Z_n u_n w_n \tag{26}$$

Neither the individual cell concentrate mass flow ($\dot{m}_{C,n}$), pulp density in the froth of the individual cell ($\rho_{f,n}$) nor the air fraction in the froth ($\epsilon_{f,n}$) are measured online at MNC. The individual cell mass flow is therefore derived empirically using the response polynomial in (21) with $P_1 \rightarrow \hat{Z}_n$ and $P_2 \rightarrow \hat{u_n}$, where the $\hat{}$ represents the modelled value. Constraints for the polynomial form of the concentrate flow model, $\dot{m}_n, = f_{3,n}(\hat{Z}_n, \hat{u}_n)$, follows. The flow of concentrate will stop when either Z or u are zero and accordingly, the model passes through the zero point. (26) also suggests that both Z and u have a positive, linear relationship with $\dot{m}_{C,n}$ as well as an interaction term, resulting in the following polynomial,

$$\dot{m}_{C,n} = d_{1,n}\hat{Z}_n + d_{2,n}\hat{u}_n + d_{5,n}\hat{Z}_n.\hat{u}_n \tag{27}$$

with $\frac{\partial \hat{\dot{m}}_{C,n}}{\partial \hat{Z}_n} > 0 \quad \forall \quad \hat{Z}_n > 0$ and $\frac{\partial \hat{\dot{m}}_{C,n}}{\partial \hat{u}_n} > 0 \quad \forall \quad \hat{u_n} > 0$.

The only measured mass flows on the concentrates are the combined mass flow of FT08 and FT09, $\dot{m}_{C1}$, and the combined concentrate of cells FT10 to FT14, $\dot{m}_{C2}$. Individual cell mass flow are therefore

determined using the respective combined mass flows,

$$\dot{m}_{C1} = \sum_{FT08}^{FT09} \dot{m}_{C,n}, \quad \dot{m}_{C2} = \sum_{FT10}^{FT14} \dot{m}_{C,n} \tag{28}$$

The objective of the training algorithm to derive $\dot{m}_{C,n}$, was to minimize the error between the sum of the modelled $\hat{\dot{m}}_{C,n}$ and measured $\dot{m}_{C1}$ and $\dot{m}_{C2}$ by changing parameters $d_{1-5,n}$ in (27). The fact that two cells contribute to the first concentrate and five cells to the second concentrate, each concentrate flow model using three parameters, d_1, d_2 and d_5, presents an over-specified solution. Since several local minimums can exists, it is possible to conclude that the majority of the mass flow is made up by just one cell. In reality, operators ensure that cells generally contribute equally down the bank. Therefore, to ensure that all the cells contribute to the combined mass flow, the training parameters of the cells that combine were kept the same. The first concentrate is calculated using only parameters d_{1_C1}, $d_{2,C1}$ and $d_{5,C1}$, in the combined first concentrate mass flow equation,

$$\hat{\dot{m}}_{C1} = d_{1,C1}(\hat{Z}_8 + \hat{Z}_9) + d_{2,C1}(\hat{u}_8 + \hat{u}_9) + d_{5,C1}(\hat{Z}_8\hat{u}_8 + \hat{Z}_9\hat{u}_9) \tag{29}$$

which is obtained via iteration by minimizing objective function,

$$J_{m1} = (\dot{m}_{C1} - \hat{\dot{m}}_{C1})^2 \tag{30}$$

Similarly, the second rougher concentrate is derived by matching all the relative individual cell mass flow parameters,

$$\hat{\dot{m}}_{C2} = d_{1,C2} \sum_{n=FT10}^{FT14} \hat{Z}_n + d_{2,C2} \sum_{n=FT10}^{FT14} \hat{u}_n + d_{5,C2} \sum_{n=FT10}^{FT14} \hat{Z}_n\hat{u}_n \tag{31}$$

and minimizing the objective function,

$$J_{m2} = (\dot{m}_{C2} - \hat{\dot{m}}_{C2})^2 \tag{32}$$

4.5. Recovery and Grade

4.5.1. Cell Recovery (R_n) and Grade (g_n)

All forms of recovery, namely, through true flotation (R_{tf}), entrainment (R_e) and total recovery (R), as well as the species' grades are determined as follows:

1. **Total cell recovery** for metal species ($R_{i,n}$) is calculated by the sum of recovery by true flotation and entrainment,

$$R_{i,n} = R_{i,e,n} + R_{i,tf,n} \tag{33}$$

2. **Recovery through true flotation** ($R_{i,tf,n}$) is determined using (6), per species,

$$R_{i,tf,n} = \frac{p_i S_{b,n} R_{f,n} \tau_{c,n}}{1 + p_i S_{b,n} R_{f,n} \tau_{c,n}} \tag{34}$$

The total mass produced from true flotation is,

$$\dot{m}_{C,tf,n} = \sum \dot{m}_{i,C,tf,n} \tag{35}$$

The mass contributed to the concentrate from true flotation for a species i is,

$$\dot{m}_{i,C,tf,n} = R_{i,tf,n}.\dot{m}_{i,F,n} \tag{36}$$

with,

$$\dot{m}_{i,F,n} = g_{i,F,n}\dot{m}_{F,n} \tag{37}$$

3. **Recovery through entrainment** ($R_{i,e,n}$) is calculated as the ratio of mass flow due to entrainment to the total amount of mass that entered the cell,

$$R_{i,e,n} = \frac{\dot{m}_{i,C,e,n}}{\dot{m}_{i,F,n}} \tag{38}$$

$\dot{m}_{i,F,n}$ is given in (37) while the mass recovered via entrainment is calculated by a mass balance, first calculating the total mass produced to concentrate by entrainment,

$$\dot{m}_{C,e,n} = \dot{m}_{C,n} - \dot{m}_{C,tf,n} \tag{39}$$

The derivation of $\dot{m}_{C,n}$ is explained in Section 4.4 and $\dot{m}_{C,tf,n}$ in (35). The mass flow of the mineral species reporting to the concentrate via entrainment is then calculated by,

$$\dot{m}_{i,C,e,n} = g^*_{i,T,n}.\dot{m}_{C,e,n} \tag{40}$$

where $g^*_{i,T,n}$ is the grade of the mineral in the pulp after true recovery,

$$g^*_{i,T,n} = \frac{\dot{m}_{i,F,n} - \dot{m}_{i,C,tf,n}}{\dot{m}_{F,n} - \dot{m}_{C,tf,n}} \tag{41}$$

4. **Concentrate grade** of every component for the individual cell ($g_{i,C,n}$) is determined using the total concentrate produced per cell ($\dot{m}_{C,n}$) and the mass recovered by both entrainment and true recovery i,

$$g_{i,C,n} = \frac{\dot{m}_{i,C,tf,n} + \dot{m}_{i,C,e,n}}{\dot{m}_{C,n}} \tag{42}$$

Note that total flow of the first cell, $\dot{m}_{F,FT08}$ and, all the various components are given. The mass flows of the subsequent cells are therefore also determined through mass balance and the method described above,

$$\dot{m}_{i,F,n+1} = \dot{m}_{i,F,n} - \dot{m}_{i,C,n} \tag{43}$$

4.5.2. Froth Recovery (R_f)

The literature mentions several, often complex and laboratory intensive, models for froth recovery. Alves et al. [1] suggested the more simplistic derivation of R_f, (10), and showed relatively good correlation to plant data. The causal model, therefore also uses this form with only β, a froth stability parameter, as unknown. Barbian et al. [3], also used a stability parameter, β, to show that the air recovery, α, decreases linearly as froth stability decreases when air flow in increased. Hadler and Cilliers [16] showed that this linearity is not preserved at lower air flows as α starts to decrease due to a decrease in froth mobility. It stands to reason, however, that the dynamic froth stability, described by Bikerman [7], will continue to increase and remain linear with respect to β in the range of operation. The causal model therefore uses the dynamic froth stability modified to include J_g instead of air flow rate by substituting $q_p \approx J_g.A$ into (12),

$$\Sigma_n \approx \frac{Z_n}{J_{g,n}} \tag{44}$$

with,

$$\beta_n = c\Sigma_n \tag{45}$$

where c becomes a linear calibration parameter, named the froth stability calibration parameter, that scales Σ to β. Only one value for c is defined for an entire bank and is the only parameter that needs to be empirically fitted in determining $R_{f,n}$. The fitting of c is discussed in Section 4.5.4. The parameters used to determine the froth recovery, upstream in the causal diagram, are:

1. **Froth residence time (FRT_n)** is determined by (8) using an assumed gas holdup (ϵ). Ventura-Medina et al. [27] mentioned that a copper ore solids bubble loading at froth depths and air rate similar to the MNC operation (approximately 0.1 m and 0.012 m/s, respectively) is between 95 % and 98 %. For this work however, ϵ_f is approximated for the MNC ore at 97 %.

2. **Froth Volume** ($V_{froth,n}$) per cell is calculated using the froth depth and the cell specifications for a cylindrical cell without froth crowders,

$$V_{froth} = \frac{\pi}{4} d_n^2 h_n \tag{46}$$

3. **Volumetric froth flow rate** ($q_{C,n}$) is calculated using the modelled mass flow and density of concentrate,

$$q_{C,n} = \frac{\hat{\dot{m}}_{C,n}}{\hat{\rho}_{C,n}} \tag{47}$$

4. **Concentrate density** ($\rho_{C,n}$) are empirically derived by fitting the combined concentrates density (ρ_{C1} and ρ_{C2}), which is measured, and assuming the individual cell densities are equal,

$$\rho_{C1} = \rho_{C,FT8} = \rho_{C,FT9} \quad , \quad \rho_{C2} = \rho_{C,FT10} = ... = \rho_{C,FT14} \tag{48}$$

The PAR observations by Hadler et al. [15], [17], [18] that describes the trade-off between froth stability and froth mobility is again used to explain the expected model for concentrate density. As air increases, solids on the bubble will increase but mobility will decrease. Higher air would increase mobility but reduce stability leading to increased solids loss and a peak in density is therefore expected. A linear empirical form of the density model is used to reduce complexity. The coefficients associated with $J_{g,n}$ are therefore expected to be either positive or negative depending on the operating region of the air flow. Similar density behaviour is expected with froth depth. Furthermore, Yianatos et al. [33] indicates that bubble loading increases with an increase in feed density signalling a positive coefficient,

$$\hat{\rho}_{C1} = q_0 \rho_F + q_1 J_{g,FT08} + q_2 J_{g,FT09} + q_3 h_{FT08} + q_4 h_{FT09} \tag{49}$$

where $0 < q_0$. The equation for the second concentrate is identical save for eleven coefficients, namely, the inputs $\rho_{F,10}$, $J_{g,FT10-FT14}$ and $h_{FT10-14}$. The objective function that is minimized by coefficients q_n is then,

$$J_{\rho_{C1}} = \sum (\rho_{C1} - \hat{\rho}_{C1})^2 \tag{50}$$

and,

$$J_{\rho_{C2}} = \sum (\rho_{C2} - \hat{\rho}_{C2})^2 \tag{51}$$

4.5.3. Floatability (p_i) and Mass Fraction (x_i)

1. **Floatability**. Welsby et al. [31] describes floatability as "a mathematically grouped set of particles that display a similar flotation rate". No other commonality between these particles need occur in order to fall within the same discrete floatability class. The floatability component method (FCM), described by Welsby et.al, [31], defines a fixed floatability value for every component (p_i) but considers the amount of mass characterized by it to vary. This method was used to determine the floatability and mass fraction of the nine species considered in the causal model, per floatable class ($p_{i,j}$ and $x_{i,j}$), as it appeared in the feed during a 2015 plant survey (Table 2).

Table 2: Component floatability and respective mass fractions as found using the FCM.

	platinum		palladium		gangue	
	p	x	p	x	p	x
fast-float	0.00432	0.52	0.00196	0.51	-	0.00
slow-float	0.00010	0.24	0.00011	0.29	2.8E-05	0.12
non-floatable	0.0	0.24	0.0	0.20	0	0.88

As the floatability is kept constant, an online method to determine the fraction of each component in the feed had to be derived for the causal model.

2. **Mass Fraction**. From an early stage in the project it was evident that the residence time, bubble surface area flux and floatability in Table 2, at fairly modest froth recovery estimates, was sufficient to ensure the recovery of all floatable platinum and palladium. It is therefore postulated that the remaining metal in the circuit tail is merely the amount of material entering the circuit less the floatable fraction in the feed or simply non-floatable material in the circuit. Note that this is only true for the higher floatable metal species, platinum and palladium, but not for the gangue. Therefore, for platinum (palladium derived similarly),

$$\dot{m}_{pt,T} = g_{pt,T}\dot{m}_T = \dot{m}_{pt,nf,F} = x_{pt,nf,F}g_{pt,F}\dot{m}_F \tag{52}$$

Rewritten as subject $x_{pt,nf,F}$,

$$x_{pt,nf,F} = \frac{g_{pt,T}\dot{m}_T}{g_{pt,F}\dot{m}_F} \tag{53}$$

Note that the feed component assays ($g_{i,F}$) and the feed mass flow ($\dot{m}_F$) are exogenous variables, known to the causal model. The tails grade assay ($g_{pt,T}$) and mass flow ($\dot{m}_T$) are however endogenous variables and although measured in the circuit, are not available to calculate the components' mass fractions. The mass flow of the tails is, however, independent of recovery and calculated as explained in Section 4.4. To determine $g_{pt,T}$, without using the recovery track in the causal model, a hypothesis was tested that the component concentration in the tail is a linear function of the same component concentration in the feed,

$$g_{pt,T} \approx m_{pt}g_{pt,F} \tag{54}$$

where m_{pt} is the slope of the function and a training parameter to minimize the objective function, $J_{pt,T}$, such that,

$$J_{pt,T} = (g_{pt,T} - \hat{g}_{pt,T})^2 \tag{55}$$

The accuracy of this hypothesis for the combined two elements (2E) in the model, platinum and palladium, was trained over the month of June 2019 and tested for the first 7 days in July 2019. This is also the period where the APBS was used to determine the J_g and d_{32} relationships to air flow. The comparison between $g_{2E,T}$ and $\hat{g}_{2E,T}$ is shown in Fig. 9 with the resulting regression statistics shown in Table 3. Considering the simplicity of the model, a fairly good representation of the real data was achieved with $R^2_{90} = 0.55$ for training and $R^2_{90} = 0.45$ testing data sets, respectively. Note that $RRMSE_{90}$ in this case is presented as the percentage of the tails grade median in order to preserve the anonymity of the grade data.

Table 3: Goodness-of-fit statistics of the 2E tails assay model.

	$g_{2E,T}$	
	Train	Test
$RRMSE_{90}$ (%)	0.11	0.15
R^2_{90}	0.55	0.45

Once $x_{pt,nf,F}$ is determined (35) the fractions of the floatable components in the feed is then given by,

$$x_{pt,ff,F} + x_{pt,sf,F} = 1 - x_{pt,nf,F} \tag{56}$$

An assumption is made that the ratio of fast to slow floatable material, as found during the 2015 survey, is constant,

$$\frac{x_{i,ff,F}}{x_{i,sf,F}} = \frac{x^o_{i,ff,F}}{x^o_{i,sf,F}} \tag{57}$$

where x^o represents the mass fraction observed during the sampling campaign in 2015.

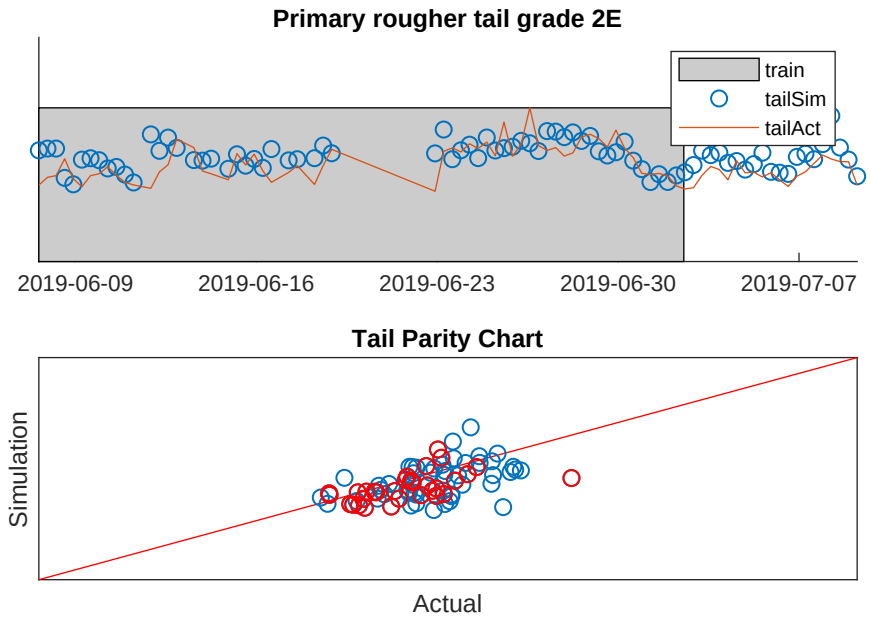

Figure 9: The time based and parity comparison plots of the primary rougher 2E tail (platinum and palladium).

4.5.4. Deriving the Froth Stability Calibration Parameter c

The hypothesis in (54) is established to derive all mass fractions in (53) and (56) and is only valid if the froth recoveries are such that all floatable material is removed. The froth stability calibration parameter c, for the rougher bank, remains the only parameter that needs to be fitted in order to obtain the froth recovery of the individual cells ($R_{f,n}$). According to (10) and (45), the froth recovery is related to β by an exponential decay as c is increased. It is therefore concluded that values above the critical c value will result in an inadequate R_f to support this hypothesis. This point is named the critical froth stability calibration parameter (c_{crit}). Froth recovery achieved at $c < c_{crit}$ is considered sufficient to not affect the quality of the $\hat{g}_{i,T}$ model. As c increases, the froth recovery will decrease to a point where more floatable material will pass to the tail, rendering the hypothesis untrue. c_{crit} is therefore defined as a sensitivity parameter used to set the tolerance for floatable material loss to the tail. Fig. 10 shows a sharp decline in R^2_{90} as c is increased past c_{crit} which for the purposes of this study was set to reflect 90 % of the highest R^2_{90} achieved, $c_{crit} = 3.2 \times 10^{-3}$. To define a more quantitative value c, for a flotation bank, a grade assay of any cell down the bank is required. Parameter c is then determined iteratively by reducing error between the measured and modelled concentrate 2E grade. More specifically, minimizing the objective function,

$$J_{grade} = (g_{2E,n} - \hat{g}_{2E,n})^2 \tag{58}$$

with constraint $c < c_{crit}$

5. Validation of the Mogalakwena North Model

The causal model of flotation was trained for the period 7 June 2019 to 2 July 2020, which is the same period as the J_g sampling campaign. The resulting model was tested on a nine day period from 2 to 11

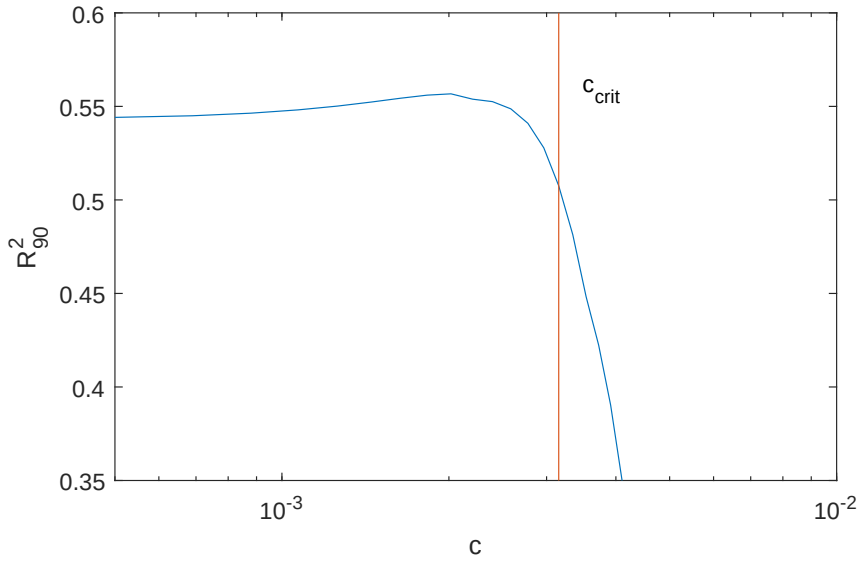

Figure 10: The robust coefficient of determination, R^2_{90}, of the tails assay to the froth stability calibration parameter, c. c_{crit}, is also shown at a value approximately 3.2×10^{-3}.

July 2020. Data sources used to derive the model are: 1) J_g and d_{32} from a manual APBS samples, 2) Z and u from the online camera information, 3) several parameters were calculated and tested against online plant data (ρ_C, n, $\dot{m}_c$), 4) the floatability of the ore and ratio of fast to slow floating metal was determined during a plant survey in 2015, 5) metal accounting assays of the circuit feed and tail were used to model the amount metal removed and lastly 6) a grade model from a sampling campaign by Venkatesan et al. [26] was used as an illustration on how to calibrate the metal gradient down the bank by training the one froth stability calibration parameter, c.

5.1. Froth Froth Velocity (u_n) and Height (Z_n)

Froth velocity (u_n) and froth height (Z_n) are empirically fitted to data by changing parameters $a_{1,3,5,n}$ and $b_{1,2,3,4,5,n}$ in (22) and (24) to minimize objective functions, (23) and (25) respectively. Plots of the inputs to the model, $J_{g,n}$ and h_n, are given in the Appendix (Fig. 20). A summary of the statistics, reporting the $RRMSE_{90}$ and the R^2_{90} for Z_n and u_n is presented in Tables 5 and 4. R^2_{90} values between 0.77 and 0.92 were observed on the first three cells' modelled velocity for both testing and training sets. The relative error for u, expected on these cells, is between 12.5 % and 21.9 %. Cell FT9 produced the best regression statistics for froth velocity during both periods. Model quality in terms of both $RRMSE_{90}$ and R^2_{90} deteriorated down the bank for both training and testing data. Similarly, regression statistics for the froth height show more accurate models on the first three cells with $R^2_{90} \geq 0.84$ and $RRMSE_{90} < 16.1\,\%$ for both training and testing periods. Errors lower than 12.4 %, relative to the median of Z_n, is expected for the training period. Relative errors increase steadily to 28.9 % for the training period and to 44.5 % for the testing period. A similar degradation in regression statistic $R^2_{90,n}$ is observed for both training and testing periods with $R^2_{90,FT14} = 0.62$ and 0.36 respectively. This decrease in predictability down the bank is possibly due to the varying removal of floatable material at the head of the bank leading to more varying froth structures. This is postulated to lead to less responsive model behaviour of Z and u to J_g and h, lower down the bank.

Table 4: Goodness-of-fit statistics of the u model, training and testing data comparison.

Train	FT8	FT9	FT10	FT11	FT12	FT13	FT14
$RRMSE_{90}$ (%)	20.7	15.9	19.9	30.4	40.1	25.2	25.2
R_{90}	0.85	0.88	0.77	0.63	0.62	0.71	0.69
Test							
$RRMSE_{90}$ (%)	21.9	12.5	15.3	15.0	31.0	28.2	22.2
R_{90}	0.77	0.92	0.89	0.83	0.59	0.65	0.77

Table 5: Goodness-of-fit statistics of the Z model, training and testing data comparison.

Train	FT8	FT9	FT10	FT11	FT12	FT13	FT14
$RRMSE_{90}$ (%)	12.4	12.2	11.3	16.9	20.6	25.9	28.9
R_{90}	0.86	0.87	0.90	0.83	0.73	0.65	0.62
Test							
$RRMSE_{90}$ (%)	16.1	13.9	12.9	15.9	22.6	35.9	44.5
R_{90}	0.84	0.87	0.89	0.84	0.70	0.46	0.36

Model comparison plots for the polynomial models of Z and u are presented in Figs. 11 and 12 respectively. The plots are presented per cell with a variable over time plot and a parity plot, comparing the actual data (y) to the modelled values ($\hat{y}$) for both training and testing periods. A more detailed discussion on the down-the-bank (dtb) behaviour of the causal model parameters is presented in the subsequent section. It is however observed that froth mobility decreases down the bank with the first three cells showing higher velocity than the last four cells. Most notably is the lowest velocity observed on FT11, the middle cell in the bank. Contrary, the height above the lip increases steadily down the bank, also becoming more variable.

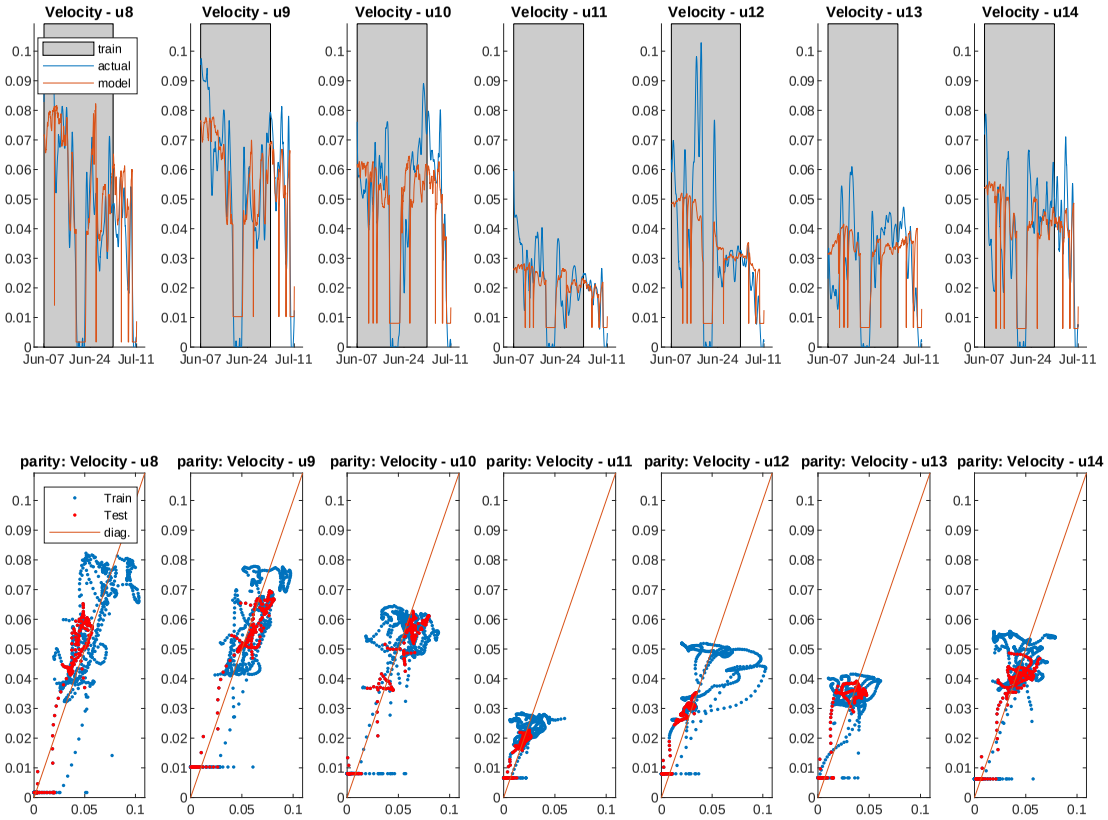

Figure 11: The time based and parity comparison plots of the froth velocity polynomial models for the primary rougher bank FT08 - 14.

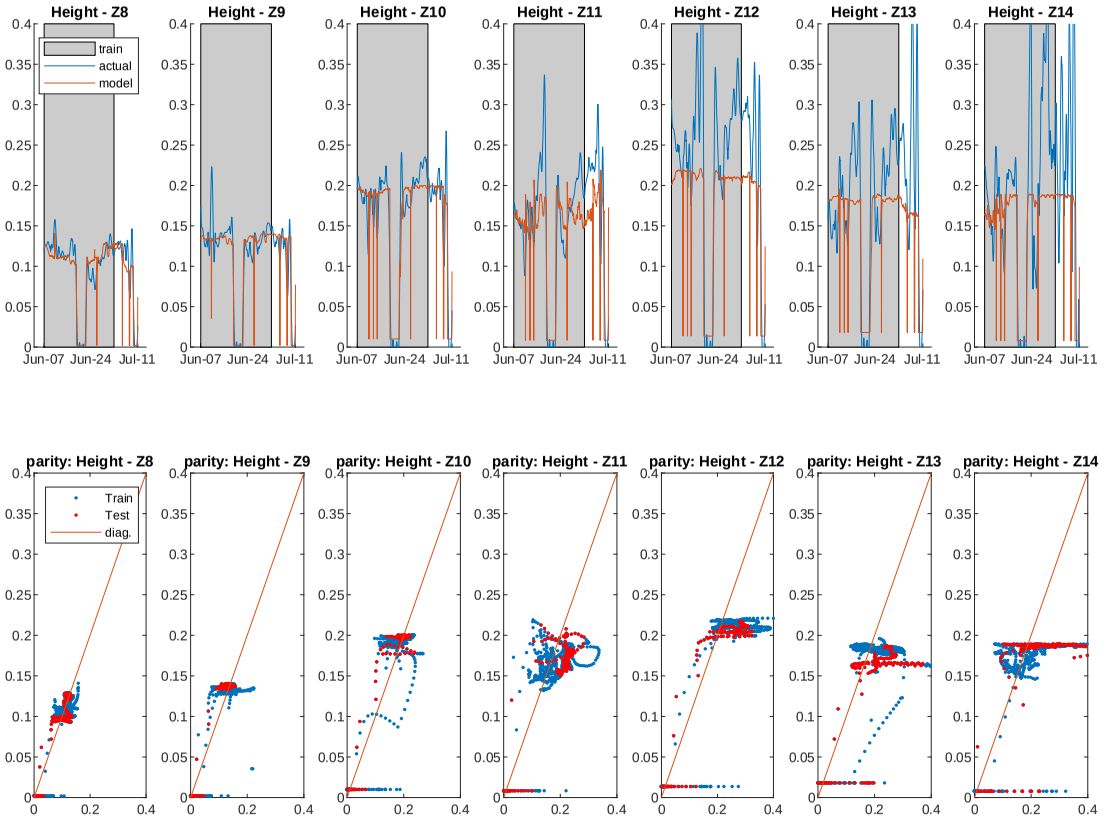

Figure 12: The time based and parity comparison plots of the height above the lip polynomial models for the primary rougher bank FT08 - 14.

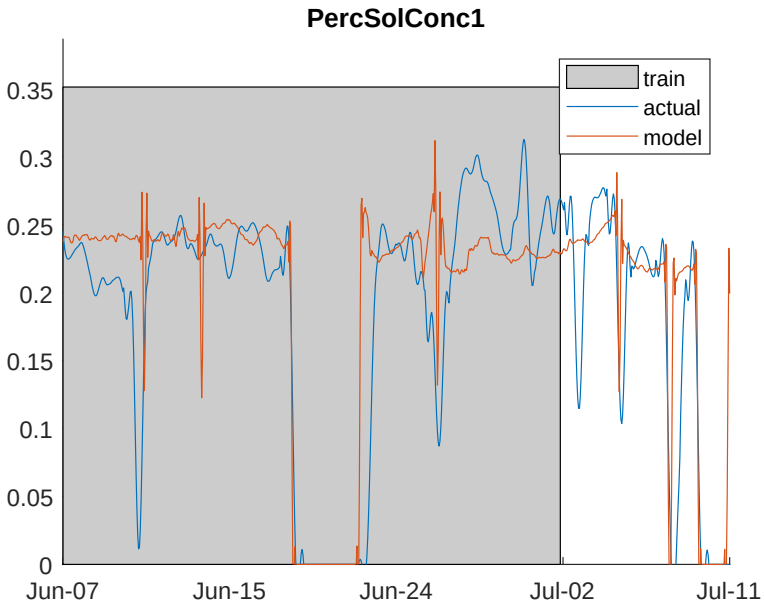

Figure 13: The 1st concentrate density polynomial models for the primary rougher bank FT08 to FT09.

The model statistics for the velocity at the free surface reported good correlation coefficients for the training data on the first three and last two cells (FT08, FT09, FT10, FT13 and FT14). Moderate quality models were obtained for FT11 and FT12 during this period. Good to moderate results were obtained during the testing period, albeit slightly lower. A significant reduction in the correlation coefficient from 0.82 to 0.13 was observed on the first cell, which is a concern.

5.2. Concentrate Density ($\rho_{C,n}$) and Mass Flow ($\dot{m}_C$)

Regression statistics of the density for the two combined concentrate streams are shown in Table 6 with time variant plots in Figs. 13 and 14. $R^2_{90} > 0.90$ and $R^2_{90} > 0.84$ were obtained for the $\rho_{C1,C2}$ during the training and testing periods, respectively. A notably lower relative error of 5 % was observed during model training for ρ_{C2} with an expected higher relative error during the testing period of 17.3 %. Relative errors observed for the ρ_{C1} during model training and testing periods were 11.6 % and 13.9 %, respectively. The model coefficients, q_n, are given in Tables 11 and 12 in the Appendix. Note that the coefficients for the froth depth were insignificant, $< 1 \times 10^{-4}$, indicating that density is mostly driven by air in the current operating region. These coefficients are therefore omitted from the table.

Table 6: Goodness-of-fit statistics of the ρ_C model comparison for the train and test data set of the primary rougher 1^{st} and 2^{nd} concentrate.

	ρ_{C1}		ρ_{C2}	
	Train	Test	Train	Test
$RRMSE_{90}$ (%)	11.6	13.9	5.1	17.3
R_{90}	0.91	0.90	0.98	0.84

Regression statistics of the mass flows for the two combined concentrate streams $\dot{m}_{C1}$ and $\dot{m}_{C2}$ are provided in Table 7. R^2_{90} values of 0.90 and 0.96 for the mass flows of the two concentrate streams were achieved during the training period. Test data statistics displayed a reduction in R^2_{90} to 0.82 and 0.79

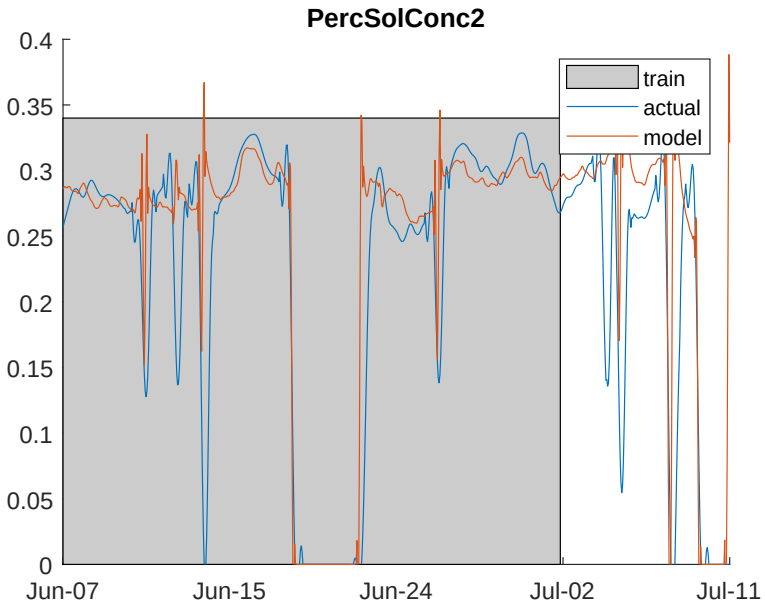

Figure 14: The 2nd concentrate density polynomial models for the primary rougher bank FT10 to FT14.

respectively. The errors relative to the mass flow median for the training period was 11.7 % and 7.4 % respectively, while the testing period was 18.9 % and 19.1 %. Figs. 15 and 16 show the time dependent plots for $\dot{m}_{C1}$ and $\dot{m}_{C2}$.

Table 7: Goodness-of-fit statistics of the $\dot{m}_C$ model comparison for the train and test data set of the primary rougher 1st and 2nd concentrate.

	$\dot{m}_{C1}$		$\dot{m}_{C2}$	
	Train	Test	Train	Test
$RRMSE_{90}$ (%)	11.7	18.9	7.4	19.1
R_{90}	0.90	0.82	0.96	0.79

5.3. Froth Recovery

Per cell froth recovery is required to achieve the ultimate objective of modelling the individual cell grade and recovery. Section 4.5.3 describes the derivation of the tails 2E grade using a hypothesis that froth recovery is sufficient for the removal of all floatable precious metals. However, the profile of where in the circuit the metal is removed is determined by deriving the froth stability calibration parameter, c, for the bank. A minimum requirement to determine c is a grade assay of one cell down the bank which at this point of the project could not be attained. However, as an illustration of the method the grade model established by Venkatesan et al. [26] during a sampling campaign in 2013, on the third cell (FT10) of the bank, is used. The model describes the grade of FT10 in terms of superficial gas velocity, $J_{g,FT10}$, and froth depth, h_{FT10}. Inputs during the period that the APBS work was performed in June 2019 are used to construct two simulated samples for the training of the calibration parameter c, using the Venkatesan et al. [26] model for FT10. These are presented as red squares in Fig. 17. 2E grades for cell FT10, derived using the causal model with different c values as a fraction of c_{crit}, are displayed indicating a value of between $c = 0.6c_{crit} = 2.0 \times 10^{-3}$ and $c = 0.8c_{crit} = 2.6 \times 10^{-3}$ as a fairly good calibration parameter to minimize

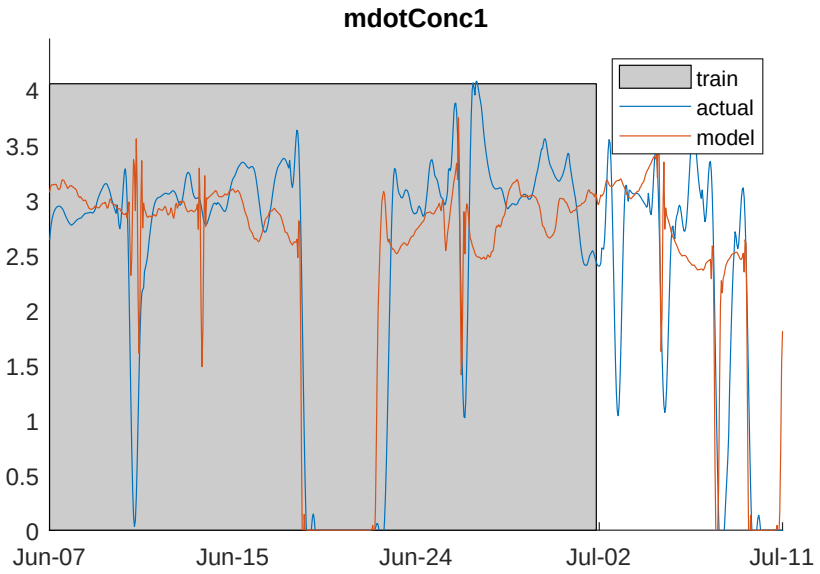

Figure 15: The 1st concentrate mass flow polynomial models for the primary rougher bank FT08 to FT09.

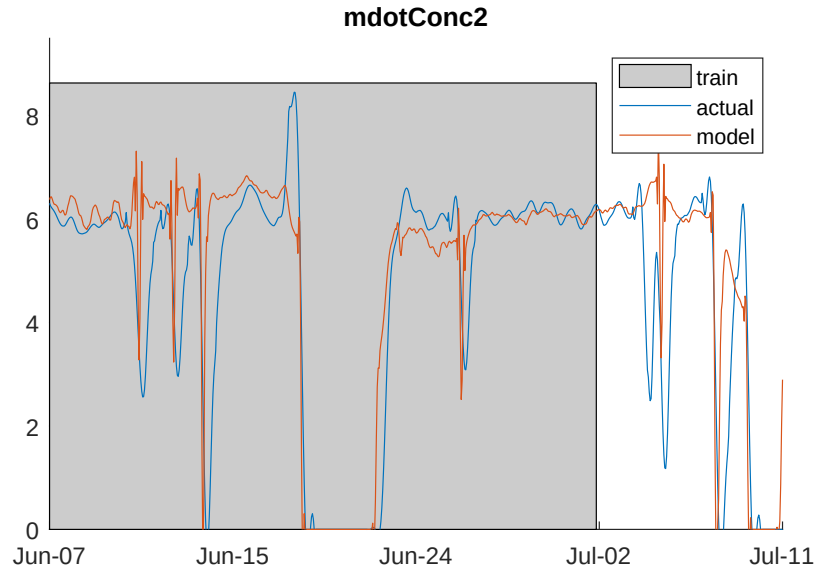

Figure 16: The 2nd concentrate mass flow polynomial models for the primary rougher bank FT10 to FT14.

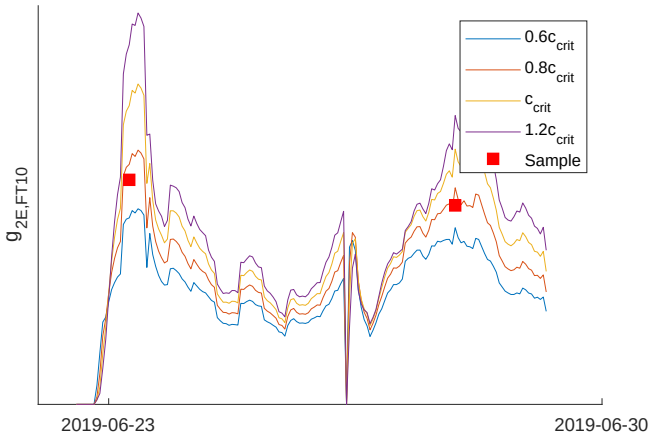

Figure 17: Effect of the froth stability calibration parameter c in terms of percentage c_{crit} on 2E grade produced by cell FT10. The two simulated samples by the Venkatesan et al. [26] model are presented as the red squares.

the objective function in (58). Going forward, an average value of $c = 0.8c_{crit} = 2.3 \times 10^{-3}$ is used. The froth recovery of every cell down the bank can thus be determined using c and Σ_n in (45) together with FRT_n in the froth recovery, (10). The resulting froth recovery down the primary rougher bank at MNC, shown in Fig. 18, indicates higher R_f for the first three cells, $0.3 < R_{f,FT8-10} < 0.6$, than the last four cells, $R_{f,FT11-14} < 0.15$. This reduction in R_f down the bank is in accordance to Hadler and Cilliers [16] observations discussed in Section 3.2. The first three cells recorded lower Bikerman froth stability parameters (Σ) and froth residence times (FRT) which result in the higher froth recovery observed. Cells FT11 to FT13 recorded significantly lower froth recoveries at $R_{f,FT11-12} < 5\,\%$ due to higher Σ ($> 25\,\text{s}$) and $FRT > 55\,\text{s}$. The froth recovery on the last cell, FT14, is again increased to 15 % due to the lowered $\Sigma \approx 10\,\text{s}$, despite the FRT remaining elevated at $\approx 65\,\text{s}$.

5.4. Down the Bank Results

The main flotation parameters calculated using the causal model are presented per flotation cell as the average for the entire period, training and testing, with error bars representing the 25 % quartile of the data spread. This is referred to as the down-the-bank data and presented in Fig. 19. The froth depth appears to be operated between 0.15 m and 0.2 m for the first three cells but shallower for FT11 at 0.13 m. Cell FT12 froth depth is operated at a similar range as the first three cells with the last two cells significantly deeper between 0.25 m and 0.30 m respectively. No discernible froth profile, as discussed by Bergh and Yianatos [5], is observed. Furthermore, the authors caution that deeper froth levels on the last cells can lead to operability issues due to the lack of floatable material. The air flow into the bank also appears to be inconsistent with the first three cells operating between 0.012 m/s and 0.017 m/s with the next three cells, FT11 to FT13, set to a significantly lower gas velocity range of between 0.005 m/s and 0.009 m/s. Cell FT14, the last cell in the bank, reported the highest gas velocity at $> 0.0175\,\text{m/s}$. The lower air input for FT11, FT12 and FT13 provides an explanation why the Bikerman stability (Σ) was higher on these cells, leading to lower froth recovery. Despite the last cell FT14 measuring the highest air flow rate, lowering Σ_{FT14} significantly, the deeper froth depth lead to a higher FRT and therefore, resulted in the lower froth recovery.

Froth height above cell lip Z_n increased steadily from FT8 to FT12, from 0.12 m to 0.28 m, and reduces to FT13 and FT14, $\approx 0.22\,\text{m}$ (Fig. 19b). A significant increase in the error of Z is observed when moving down the bank. This supports the observation that predictability is affected by floatable material being removed irregularly down the bank. Velocity down the bank is the highest on the first three cells, between

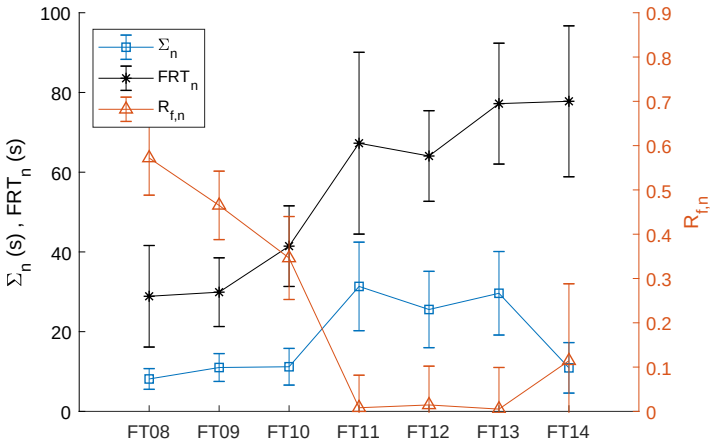

Figure 18: Down the bank results of the average Σ_n, FRT_n and $R_{f,n}$ with error bars indicating the 25 % quartile.

0.052 m/s and 0.063 m/s, dropping down the lowest velocity on FT11, 0.023 m/s, and increasing steadily again from FT12 to FT14, 0.047 m/s. Mobility of the froth is therefore better on the first part of the bank, the worst in the middle and improved towards the latter part.

Superficial gas velocity S_b, per definition, linearly follows the form of the air velocity (Fig. 19c). The solids mass flow to concentrate appears to be similar for the first three cells at approximately 1.4 t/h, decreasing significantly to 0.75 t/h for cell FT11. Cell FT12 to FT14 produced similarly at an average mass flow of between 1.2 t/h and 1.3 t/h. The lowered mass production observed on FT11 is due to the lowest velocity overall and the lowest height above the lip for the cells contributing to the 2$^{\text{nd}}$ concentrate.

Similar to observations by Hadler and Cilliers [16], the recovery of the bank was mostly achieved by the first three cells (Fig. 19d). Cells FT8 to FT10 cumulatively produces 64 % of the bank's total recovery of 64.5 %. As observed in the previous section, the contribution of FT11 and FT13 to the cumulative down the bank recovery was negligible due to the low R_f achieved on these cells. Recovery contributions by FT14 was however similarly insignificant, albeit more than FT11 and FT13. Grade down the bank drops materially after the first cell, stabilizing significantly lower from FT11 to FT14, which, produced similar grades.

The results of the recovery and grade down the bank presents cells that contribute significantly to the profitability of the plant, particularly the first three cells. However, the last four cells indicate low metal recovery values despite contributing to the 2$^{\text{nd}}$ concentrate mass flow. These cells will receive a metal concentrate upgrade in the cleaners but can potentially lead to a penalty in terms of smelting cost with no significant benefit in metal production. There might even be an argument to improve profitability of the concentrator by bypassing cells FT11 to FT13 completely due to the negligible froth recovery but cost impact of the downstream circuit due to product mass flow.

6. Conclusions

The study describes the causal flow of the flotation model from all the independent variables in the system to the individual cell outputs, recovery and grade (Fig. 6). This model structure facilitates the application of controller design and online optimization since the manipulated and disturbance variables are described as the only inputs. The model is applied to plant data on an industrial platinum concentrator using the available online data and 8-hour composite assays. No additional sampling surveys or laboratory tests are conducted to train the model, simplifying industrial application. It is acknowledged that manual APBS samples and a grade model of one cell further down the bank is required if this work is to be performed

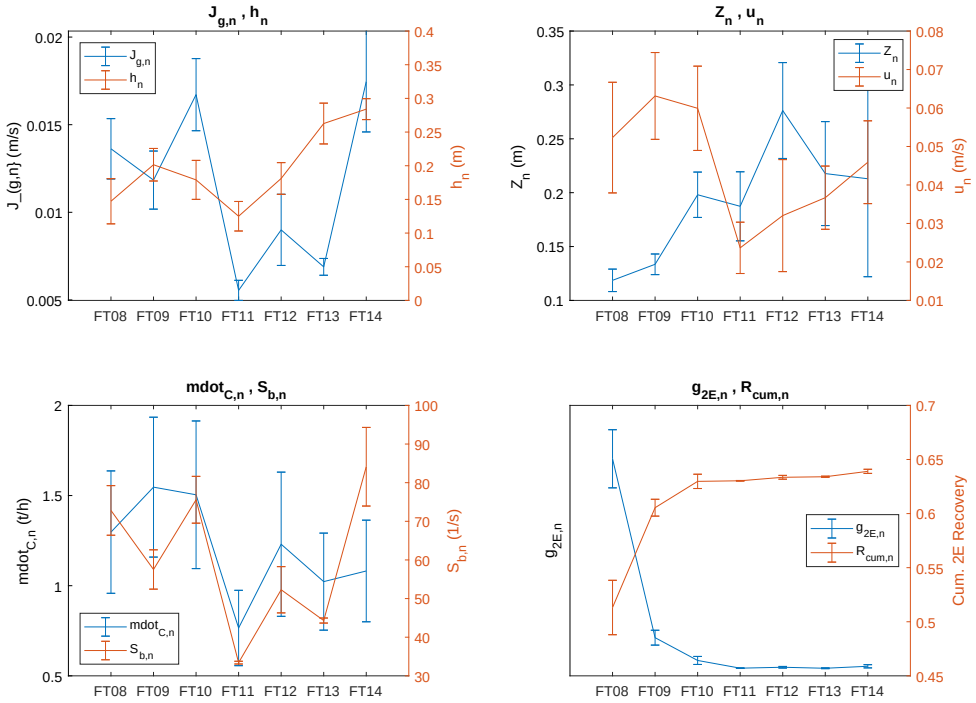

Figure 19: Down the bank results for a) inputs $J_{g,n}$ and h_n, b) froth characteristics Z_n and u_n, c) mass flow $\dot{m}_n$ and surface flux $S_{b,n}$ and d) individual cell grade $g_{2E,n}$ and cumulative recovery $R_{cum,n}$.

on another site. The regression statistics show acceptable correlation to the plant data during training and testing sets, particularly for the first three cells. Model quality is reduced towards the latter cells in the bank which agree with observations made in literature. The causal model presents an adequate characterization of the circuit and is therefore considered suitable for simulation and offline optimization. The next phase of the project will focus on the design of a steady-state optimizer subject to a financial objective, similar to the work performed by Bergh et al. [6].

References

[1] N. Alves, O. Savassi, A. Eduardo, C. Peres, and A. Henriques. Modelling flotation with a flexible approach – Integrating different models to the compartment model. *Minerals Engineering*, 66-68:68–76, 2014.

[2] N. Arbiter and C. Harris. Flotation Kinetics. *D.W. Feurstenau (Ed.) Froth Flotation, 50th Anniversary Volume*, 1962.

[3] N. Barbian, K. Hadler, E. Ventura-Medina, and J. J. Cilliers. The froth stability column: Linking froth stability and flotation performance. *Minerals Engineering*, 18(3):317–324, 2005.

[4] N. Barbian, E. Ventura-Medina, and J. J. Cilliers. Dynamic froth stability in froth flotation. *Minerals Engineering*, 16(11):1111–1116, 2003.

[5] L. Bergh and J. Yianatos. Control of rougher flotation circuits aided by industrial simulator. *Journal of Process Control*, 23(2):140–147, 2013.

[6] L. Bergh, J. Yianatos, and A. Ulloa. Supervisory control strategies evaluated on a pilot Jameson flotation cell. *Control Engineering Practice*, 90(November 2018):101–110, 2019.

[7] J. J. Bikerman. *Foams*. Springer-Verlag Berlin, 1973.

[8] L. Chen. Robust Regression and Outlier Detection with the ROBUSTREG Procedure. In *SUGI 27*, Florida, 2002. SUGI.

[9] G.S. Dobby and J.A. Finch. Column Flotation: A Selected Review, Part II. *Minerals Engineering*, 4:911–923, 1991.

[10] D. Galles and J. Pearl. Axioms of causal relevance. *Artificial Intelligence*, 97(1-2):9–43, 1997.

[11] B K Gorain, T.J. Napier-Munn, J Franzidis, and E V Manlapig. Studies on Impeller Type, Impeller Speed and Air Flow Rate in an Industrial Scale Flotation Cell. Part 5: Validation of k-Sb Relationship and effect of Froth Depth. *Minerals Engineering*, 11(7):615–626, 1998.

[12] B.K. Gorain, J.P. Franzidis, and E.V. Manlapig. Studies on impeller type, impeller speed and air flow rate in an industrial scale flotation cell. Part 3: Effect on superficial gas velocity. *Minerals Engineering*, 9(6):639–654, 1996.

[13] B.K. Gorain, J.P. Franzidis, and E.V. Manlapig. Studies on impeller in an industrial flotation cell. Part 4. Effect of bubble surface area. *Minerals Engineering*, 10(4):367–379, 1997.

[14] B.K. Gorain, M.C. Harris, J.-P. Franzidis, and E.V. Manlapig. The effect of froth residence time on the kinetics of flotation. *Minerals Engineering*, 11(7):627–638, 1998.

[15] K. Hadler. The link between froth surface grade and flotation feed grade. *Minerals Engineering*, 78:32–37, 2015.

[16] K. Hadler and J. J. Cilliers. The relationship between the peak in air recovery and flotation bank performance. *Minerals Engineering*, 22(5):451–455, 2009.

[17] K. Hadler, M. Greyling, N. Plint, and J. J. Cilliers. The effect of froth depth on air recovery and flotation performance. *Minerals Engineering*, 36-38:248–253, 2012.

[18] K. Hadler, C. D. Smith, and J. J. Cilliers. Recovery vs. mass pull: The link to air recovery. *Minerals Engineering*, 23(11-13):994–1002, 2010.

[19] R King. Model for the design and control of flotation plants. *Conference: Apcom72*, pages 341–350, 1973.

[20] Z. T. Mathe, M. C. Harris, and C. T. O'Connor. Review of methods to model the froth phase in non-steady state flotation systems. *Minerals Engineering*, 13(2):127–140, 2000.

[21] M. H. Moys. Mass Transport in Flotation Froths. *Mineral Processing and Extractive Metallurgy Review*, 5(1-4):203–228, 1989.

[22] S. J. Neethling and J. J. Cilliers. Modelling flotation froths. *International Journal of Mineral Processing*, 72(1-4):267–287, 2003.

[23] J. Pearl. Causal diagrams for empirical research. *Biometrika*, 82(4):669–688, 1995.

[24] O. Renaud and M. P. Victoria-Feser. A robust coefficient of determination for regression. *Journal of Statistical Planning and Inference*, 140(7):1852–1862, 2010.

[25] D.R. Seaman, J.-P. Franzidis, and E.V. Manlapig. Bubble load measurement in the pulp zone of industrial flotation machines – a new device for determining the froth recovery of attached particles. *International Journal of Mineral Processing*, 74:1–13, 2004.

[26] L. Venkatesan, A. Harris, and M. Greyling. Optimisation of air rate and froth depth in flotation using a CCRD factorial design - PGM case study. *Minerals Engineering*, 66:221–229, 2014.

[27] E. Ventura-Medina, N. Barbian, and J. J. Cilliers. Solids loading and grade on mineral froth bubble lamellae. *International Journal of Mineral Processing*, 74(1-4):189–200, 2003.

[28] E. Ventura-Medina and J. J. Cilliers. A model to describe flotation performance based on physics of foams and froth image analysis. *International Journal of Mineral Processing*, 67(1-4):79–99, 2002.

[29] M. A. Vera, J. P. Franzidis, and E. V. Manlapig. Simultaneous determination of collection zone rate constant and froth zone recovery in a mechanical flotation environment. *Minerals Engineering*, 12(10):1163–1176, 1999.

[30] M. A. Vera, Z. T. Mathe, J. P. Franzidis, M. C. Harris, E. V. Manlapig, and C. T. O'Connor. The modelling of froth

zone recovery in batch and continuously operated laboratory flotation cells. *International Journal of Mineral Processing*, 64(2-3):135–151, 2002.

[31] S. D.D. Welsby, S. M.S.M. Vianna, and J. P. Franzidis. Assigning physical significance to floatability components. *International Journal of Mineral Processing*, 97(1-4):59–67, 2010.

[32] F. Yang, P. Duan, S. L. Shah, and T. Chen. *Capturing connectivity and causality in complex industrial processes*. Number 9783319053790. Springer, 2014.

[33] J. Yianatos, M. Moys, F. Contreras, and A. Villanueva. Froth recovery of industrial flotation cells. *Minerals Engineering*, 21(12-14):817–825, 2008.

7. Appendix

Table 8: Nomenclature table of the causal model of Flotation.

Symbol	Description	Unit
p	Mineral flotability	dimensionless
d	Diameter	m
h_{max}	Height of cell	m
$\dot{m}$	Mass flow	kg/s
q	Volumetric flow	m^3/s
Lv	Level valve opening	%
Av	Air valve opening	%
L	Cell level	%
ρ	density	t/m^3
h	Froth Depth	m
J_g	Superficial gas velocity	m/s
τ	Pulp residence time	s
u	Froth Velocity	m/s
Z	Froth height above the cell lip	m
d_{32}	Sauter mean bubble size diameter	m
S_b	Bubble surface area flux	$1/s$
Σ	Dynamic froth stability parameter	s
β	Froth stability parameter	s
FRT	Froth residence time	s
ϵ_f	Volumetric gas fraction in the froth	fraction
R	Recovery	%
w_n	Lip length of a cell	m

Suffices	
i	Mineral species
n	Cell number
k	Stream
s	Solids
w	Water
F	Feed
T	Tail
C	Concentrate
tf	True flotation
e	Entrainment

Table 9: 2-n Polynomial model coefficients for Z.

	b_0	b_1	b_2	b_3	b_4	b_5
FT08	0	0.28	6.94	-0.52	-134.4	8.50
FT09	0	0.44	13.33	-0.78	-490.8	-3.10
FT10	0	0.54	17.85	-0.96	-563.1	-2.26
FT11	0	2.29	35.13	-3.07	-1989.6	-269.08
FT12	0	1.05	21.59	-1.69	-497.7	-45.24
FT13	0	0.27	33.49	-0.60	-1973.8	9.81
FT14	0	0.35	7.23	-0.71	-420.0	29.14

Table 10: 2-n Polynomial model coefficients for u.

	a_0	a_1	a_2	a_3	a_4	a_5
FT08	0	0	5.47	0	-7.22	-7.25
FT09	0	0	6.74	0	-35.07	-4.92
FT10	0	0	4.33	0	-48.61	-0.19
FT11	0	0	4.73	0	-1.93	-2.56
FT12	0	0	4.36	0	-39.00	-0.16
FT13	0	0	8.07	0	-3.84	-10.89
FT14	0	0	3.26	0	-46.66	-0.09

Table 11: Coefficients for the 1st combined concentrate density models.

	q_0	q_1 $(J_{g,FT8})$	q_2 $(J_{g,FT9})$
ρ_{C1}	0.0003	9.5	-8.2

Table 12: Coefficients for the 2nd combined concentrate density models.

	q_0 ($\rho_{F,FT10}$)	q_1 ($J_{g,FT10}$)	q_2 ($J_{g,FT11}$)	q_3 ($J_{g,FT12}$)	q_4 ($J_{g,FT13}$)	q_5 ($J_{g,FT14}$)
ρ_{C2}	0.0001	3.5	-20.0	5.1	-11.6	-2.5

Table 13: 2-n Polynomial model coefficients for $\dot{m}_{C,n}$.

	d_0	d_1	d_2	d_3	d_4	d_5
FT08	0	48.5	1.2	0	0	-5.2
FT09	0	48.5	1.2	0	0	-5.2
FT10	0	7.5	-65.9	0	0	684.1
FT11	0	7.5	-65.9	0	0	684.1
FT12	0	7.5	-65.9	0	0	684.1
FT13	0	7.5	-65.9	0	0	684.1
FT14	0	7.5	-65.9	0	0	684.1

Table 14: Coefficients for the combined concentrate density models.

	q_0	q_1 ($J_{g,FT8}$)	q_2 ($J_{g,FT9}$)			
ρ_{C1}	0.0003	9.5	-8.2			
	q_0 ($\rho_{F,FT10}$)	q_1 ($J_{g,FT10}$)	q_2 ($J_{g,FT11}$)	q_3 ($J_{g,FT12}$)	q_4 ($J_{g,FT13}$)	q_5 ($J_{g,FT14}$)
ρ_{C2}	0.0001	3.5	-20.0	5.1	-11.6	-2.5

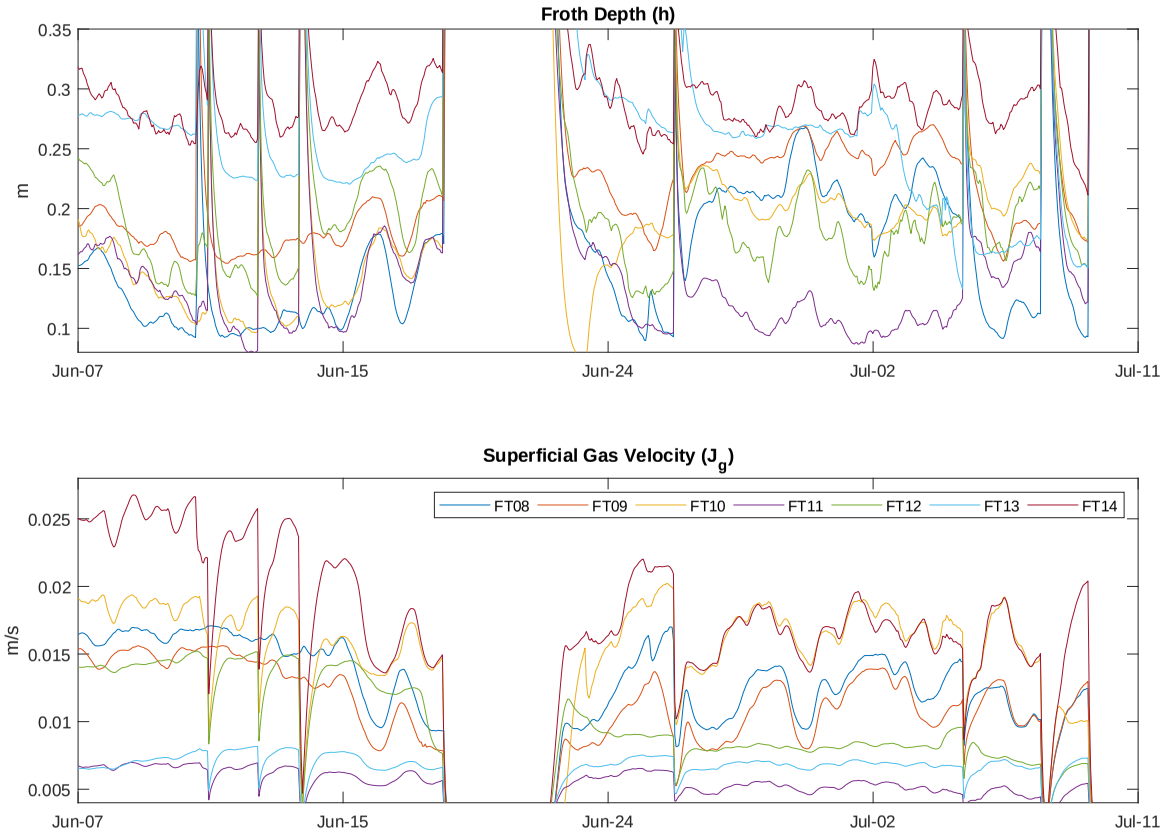

Figure 20: The time based plots of the froth depth h and the superficial gas velocity J_g for the primary rougher bank FT08 - FT14.